

## A 3D feature point tracking method for ion radiation

Kouwenberg, Jasper J M; Ulrich, Leonie; Jäkel, Oliver; Greilich, Steffen

**DOI**

[10.1088/0031-9155/61/11/4088](https://doi.org/10.1088/0031-9155/61/11/4088)

**Publication date**

2016

**Document Version**

Accepted author manuscript

**Published in**

Physics in Medicine and Biology

**Citation (APA)**

Kouwenberg, J. J. M., Ulrich, L., Jäkel, O., & Greilich, S. (2016). A 3D feature point tracking method for ion radiation. *Physics in Medicine and Biology*, 61(11), 4088-4104. <https://doi.org/10.1088/0031-9155/61/11/4088>

**Important note**

To cite this publication, please use the final published version (if applicable). Please check the document version above.

**Copyright**

Other than for strictly personal use, it is not permitted to download, forward or distribute the text or part of it, without the consent of the author(s) and/or copyright holder(s), unless the work is under an open content license such as Creative Commons.

**Takedown policy**

Please contact us and provide details if you believe this document breaches copyrights. We will remove access to the work immediately and investigate your claim.

## A 3D Feature Point Tracking Method for Ion Radiation

*Kouwenberg, Jasper J.M.<sup>1,\*</sup>, Ulrich, Leonie<sup>2,3</sup>, Jäkel, Oliver<sup>2,3,4</sup>, Greilich, Steffen<sup>2,3</sup>*

<sup>1</sup> *Radiation, Science & Technology, Delft University of Technology, Mekelweg 15, 2629 JB Delft, Netherlands*

<sup>2</sup> *Division of Medical Physics in Radiation Oncology, German Cancer Research Center (DKFZ), Im Neuenheimer Feld 280, 69120 Heidelberg, Germany*

<sup>3</sup> *Heidelberg Institute for Radiation Oncology (HIRO), National Center for Radiation Research in Oncology, Im Neuenheimer Feld 280, 69120 Heidelberg, Germany*

<sup>4</sup> *Heidelberg Ion-Beam Therapy Center (HIT), Im Neuenheimer Feld 450, 69120 Heidelberg, Germany*

### **Abstract**

A robust and computationally efficient algorithm for automated tracking of high densities of particles travelling in (semi-) straight lines is presented. It extends the implementation of (Sbalzarini & Koumoutsakos 2005) and is intended for use in the analysis of single ion track detectors. By including information of existing tracks in the exclusion criteria and a recursive cost minimization function, the algorithm is robust to variations on the measured particle tracks. A trajectory relinking algorithm was included to resolve the crossing of tracks in high particle density images. Validation of the algorithm was performed using Fluorescent Nuclear Track Detectors (FNTD) irradiated with high- and low (heavy) ion fluences and showed less than 1% faulty trajectories in the latter.

### **Keywords**

Proton and ion radiotherapy, fluorescent nuclear track detectors, FNTD, ImageJ, Fiji

### **1. Introduction**

The therapeutical use of (heavy) charged particles such as protons, helium or heavier ions in external radiotherapy has gained increased attention over the last years (Nelson 2015; Hanin & Zaider 2014; Loeffler & Durante 2013). In addition, alpha emitters are steadily gaining importance in radionuclide therapy and are even explored in clinical trials (Elgqvist et al. 2014; de Kruijff et al. 2015; Jadvar & Quinn 2013; Sartor et al. 2012; Kratochwil et al. 2014). The cell killing efficiency per

\* Corresponding author: [j.j.m.kouwenberg@tudelft.nl](mailto:j.j.m.kouwenberg@tudelft.nl)

deposited energy by these radiation types can differ significantly from that of mega-voltage X-ray or electrons. This hampers the transfer of clinical experience in dosage and calls for new reference data. Due to the large variation in energy deposition by single ions on micrometer scales, these data have also to be acquired on a cellular level using suitable detector systems. One example for such assays is the Cell-Fit-HD which relies on the use of Fluorescent Nuclear Track Detectors (FNTD) (Niklas, Greilich, et al. 2013; Niklas, Melzig, et al. 2013) to record 3D data on the path and the energy loss of individual ions. Spatial resolution in the (sub)micrometer range can be achieved in this case when applying confocal laser scanning microscopy for read-out. Other examples include semiconductor detectors and the work done using microbeam facilities (Grad et al. 2012; Prise & Schettino 2011; Hei et al. 2009; Schettino et al. 2010).

The relatively low cost, biocompatibility and ease-of-use of these detectors result in a wide range of potential applications (Bartz et al. 2014; Klimpi et al. 2015; Akselrod et al. 2014). However, the automated identification and evaluation of ion tracks using post processing of the fluorescence image data depends significantly on dedicated tracking algorithms.

Feature point tracking, i.e. tracking of points that represent physical particles, is an area of active development with many applications from biology (Chetverikov & Verestói 1999) to computer vision (Luo et al. 2015). To the best knowledge of the authors, currently available algorithms are impractical or incompatible with the specific requirements of ion beam data such as crossing of tracks and high numbers of tracks per area. Fluences exceeding  $10^7 \text{ cm}^{-2}$ , corresponding to 1000 tracks on a  $100 \times 100 \mu\text{m}^2$  field of view, are often found in clinical beams. On the other hand, ions travel mostly in straight lines which is an excellent property to be used for discrimination between potential tracks. This property has not been fully exploited up to now.

We therefore present here an extension of the algorithm of Sbalzarini, Koumoutsakos (Sbalzarini & Koumoutsakos 2005), Levy and Incardona (Levy & Incardona 2014) and the implementation in the MOSAIC Toolsuite for ImageJ (Schneider et al. 2012) and FIJI (Schindelin et al. 2012). A robust and computationally efficient algorithm for the reconstruction of fluorescent ion tracks could be established by introducing a cost function aimed at specific characteristics of ion interactions in matter and adding both a recursive cost minimization function and a track relinking algorithm.

## 2. Method

### 2.1. Fluorescent Nuclear Track Detector

Detection of ion tracks was done using FNTDs cut from a single crystal of aluminium oxide doped with carbon and magnesium produced by Landauer Inc. (Stillwater, Oklahoma, USA). The dopants produce local charge imbalances in the lattice, known as color centers, which can trap secondary electrons induced by traversing ions and thereby undergo radiochromic transformations (Akselrod et al. 2006). Exciting the color centers with a 633 nm HeNe laser produces fluorescence at 750 nm, which allows for read out with a Confocal Laser Scanning Microscope (CLSM). The high color center density and low background fluorescence allows for a large range in detectable Lineal Energy Transfer (LET) (Bartz et al. 2014). A track of an ion is visible as a bright spot against a low intensity background, where the intensity of the spot is dependent on the LET (Niklas, Bartz, et al. 2013). We will refer to the observed spots as ‘feature points’. It is important to note that a feature point does not necessarily represent a physical particle due to the possibility of false-positive detection due to noisy or defect samples.

### 2.2. Feature point detection

This paper largely follow the notation of Sbalzarini & Koumoutsakos (2005) to enhance clarity. FNTD readout commonly yields a stack of  $n = 1 \dots N$  image slices, each  $X$  by  $Y$  pixels in size, thereby representing a volume  $V$  in the FNTD. Detection of spots in the slices was done using Levy’s algorithm for feature point extraction as found in the MOSAIC ToolSuite plugin for ImageJ and FIJI, yielding for each slice image  $A_n$  a set of feature points  $P^{A_n}$  for intensity threshold  $I$  and feature point radius  $r$ . The amount of feature points in  $P^{A_n}$  is given by  $\dim(P^{A_n})$ . Feature points are viewed in Euclidian space where  $x$  and  $y$  represent the pixel numbers in the respective directions, while  $z$  represents the depth in the image stack as given by the slice number  $n$ .

### 2.3. Feature point linking

Trajectories are formed by linking feature points in  $P^{A_n}$  to feature points in subsequent slices  $P^{A_{n+k}}$  where  $k = 1 \dots R$  and  $R$  is the user-specified link range. Due to the different focus of application, linking is done between feature points in depths (slice dimension) rather than in time (frame dimension) as in Sbalzarini & Koumoutsakos (2005). This, however, does not affect the generality of the following considerations.

By applying a cost function to each feature point combination, the cost matrix  $C^{A_n} \in \mathbb{R}^{\dim(P^{A_n}) \times \sum \dim(P^{A_{n+k}})}$  is constructed. Since the method used in this paper employs a recursive minimization function for linking instead of a common assignment problem approach, there is no longer a need for matrix filling using the dummy feature points found in Sbalzarini & Koumoutsakos (2005) when  $\dim(P^{A_n}) \neq \dim(P^{A_{n+k}})$ . The association matrix given by Sbalzarini & Koumoutsakos (2005) is replaced by an association vector  $G^{A_n} \in \mathbb{R}^{\dim(P^{A_n})}$ , containing the indices of the linked partners for the feature points in  $P^{A_n}$ . Trajectories are later extracted by following the indices in  $G^A$ . The values of  $G^{A_n}$  are set to 0 to represent the absence of links.

### 2.3.1. Linking cost function

Let  $C_{i,j}^{A_n} = \sum_{\text{feature}} \phi_{i,j}^{\text{feature}}$ . Each feature  $\phi_{i,j}^{\text{feature}}$  penalizes the mismatch of a specific characteristic between feature point  $i$  in  $P^{A_n}$  and feature point  $j$  in  $P^{A_{n+k}}$ , so that  $C_{i,j}^{A_n}$  is a compressed representation of the matching of these characteristics. Assuming each feature point  $i$  has only one true linking partner  $j$ , finding the lowest the linking cost in  $C_{i,j}^{A_n}$  for each feature point  $i$  will approximate the solution to minimizing the cost matrix, i.e.  $\sum_i \min C_{i,j}^{A_n} \approx \min \sum_i C_{i,j}^{A_n}$ , for a fraction of the calculation time. Heavy ions can safely assumed to follow an approximately straight path with constant velocity considering the typical track-lengths assessed in an FNTD, i.e. several tens of micrometers. Cumulative effects of small-angle coulomb-scattering are tolerated by the algorithm, while the frequency of large-angle events can be – even at the end of the particle range – considered to be rare and their impact on the track reconstruction (splitting of one track into two tracks with corresponding total length) as benign. Four features are used for the linking of feature points in this method. Some of these features find their basis in the work of Sbalzarini, Koumoutsakos, Levy and Incardona, but were modified to better serve the tracking of ions with these characteristics.

### 2.3.2. Features

To filter unlikely linking candidates, the first feature describes the distance between feature points which is given by the squared distance between feature points  $i$  and  $j$ .

$$\phi_{i,j}^{\text{distance}} = w_d^2 \begin{cases} |d_{i,j}|^2 + (n_j - n_i)^2, & |d_{i,j}|^2 + (n_j - n_i)^2 \leq d_{p,max} \\ \infty, & \text{elsewhere} \end{cases} \quad 1$$

Where  $w_d$  is the user-specified distance weight factor,  $d_{i,j}$  is the linking distance in the x-y plane and  $d_{p,max}$  is the user-specified maximum linking distance.

In order to favour constant intensities, the second feature is based on the likeness of the zero and second order intensity momenta.

$$\phi_{i,j}^{\text{intensity}} = \frac{w_i^2}{\pi \cdot r^2} \sum_{x=-r}^r \sum_{y=-r}^r (1 + x^2 + y^2) \cdot \begin{cases} |I_{x,y}^j - I_{x,y}^i|, & x^2 + y^2 \leq r^2 \\ 0, & \text{elsewhere} \end{cases} \quad 2$$

Where  $w_i$  is the user-specified feature weight factor,  $r$  is the feature point radius and  $I_{x,y}^p$  is the pixel intensity at position  $x, y$  from the center of feature point  $p$ .

The third feature is given as the absolute velocity difference, where  $v_{i,j}$  is the link velocity vector as given by eq. 4.

$$\phi_{i,j}^{\text{velocity}} = w_v^2 \begin{cases} \left| |v_{i,j}|^2 - |\bar{v}_i^H|^2 \right|, & |\bar{v}_i^H|^2 > 0 \\ 0, & \text{elsewhere} \end{cases} \quad 3$$

$$v_{i,j} = \begin{bmatrix} \Delta x / \Delta z \\ \Delta y / \Delta z \end{bmatrix} = \frac{1}{n_j - n_i} \begin{bmatrix} x_j - x_i \\ y_j - y_i \end{bmatrix} \quad 4$$

$w_v$  is the user-specified velocity weight factor and  $\bar{v}_i^H$  is the average link velocity vector of the last  $H$  feature points in the trajectory of feature point  $i$ , where  $H$  is specified by the user. When feature point  $i$  is not part of an existing trajectory,  $\bar{v}_i^H$  is set to zero.

The final feature is based on the angle between the  $\bar{v}_i^H$  and  $v_{i,j}$ .

$$\phi_{i,j}^{\text{angle}} = w_a^2 \begin{cases} f(\theta_{i,j})^2 & |d_{i,j}| > r_p/2, |\bar{v}_i^H|^2 > 0, |\theta_{i,j}| \leq \theta_{p,max} \\ \beta \cdot f(\theta_{p,max})^2 & |d_{i,j}| > r_p/2, |\bar{v}_i^H|^2 = 0 \\ \gamma \cdot f(\theta_{p,max})^2 & |d_{i,j}| \leq r_p/2 \\ \infty & \text{elsewhere} \end{cases} \quad 5$$

$$f(\theta_{i,j}) = \frac{\alpha}{2} [\cos \theta_{i,j} - 1] = \frac{\alpha}{2} \left[ \frac{(v_{i,j} \cdot v_i^H)}{|v_{i,j}| |v_i^H|} - 1 \right] \quad 6$$

Where  $w_a$  is the user-specified angle weight factor,  $r_p$  is the allowed particle drift, usually given by the particle radius  $r$ , and  $\theta_{p,max}$  is user-specified maximum allowed feature point linking angle. To allow for small noise variations in tracks perpendicular to the z-axis, a standard cost value is used for links with  $|d_{i,j}| \leq r_p/2$ . However, since continuation of existing tracks is favoured,  $\beta$  was chosen higher than 1. It was experimentally found by applying the method to the set of alpha tracks given in section 3.2 that  $\alpha = d_{max}$ ,  $\beta = 6/5$  and  $\gamma = 1$  were good values. Both  $\beta$  and  $\gamma$  were set (close) to 1 in order to simplify the interpretation of the angle cost factor for the user.

When the link range  $R \geq 2$ , an extra criteria is introduced in order to prevent multiple links to feature point  $j$ . If  $j \in G$ , i.e. feature point  $j$  has already been linked to from one of the previous image slices, and the current link  $C_{i,j}^{A_n}$  exceeds the cost of the previous link, then  $C_{i,j}^{A_n}$  is to  $\infty$  to prevent suboptimal replacements of links during feature point linking.

### 2.3.3. Link Cost Minimization

Feature point linking is performed by applying a recursive minimization function which aims to find the best linking candidate  $i$  for each feature point  $j$  in  $P^{A_n+k}$ , given that each feature point can only be linked once. When feature point  $i$  was already linked, i.e.  $G_i^{A_n} > 0$ , and the cost for linking feature point  $j$  to  $i$  is lower than the cost of the existing link, the existing link is replaced and the function calls itself to find the next best link for delinked feature point  $j = G_i^{A_n}$  in  $P^{A_n+k}$ . This process is halted when no new link with cost lower than  $C_{max}$ , the maximum allowed linked cost, which was experimentally chosen as  $4 d_{p,max}^2$ , can be found. A pseudo-code representation of the function is given below.

**Function** FindBestLink (feature point  $j$ )

$cost = C_{max}$ ,  $candidate = -1$

**for each** feature point  $i$  **do**

**if**  $C_{i,j}^{A_n} < cost$  &&  $C_{i,j}^{A_n} < C_{i,G_i^{A_n}}^{A_n}$  **then**

$candidate = i$ ,  $cost = C_{i,j}^{A_n}$

**end**

**if**  $candidate == -1$  **then**

no link found, return

```

if  $G_{\text{candidate}}^{A_n} == -1$  then
     $G_{\text{candidate}}^{A_n} = j$ , return
else then
     $old\_j = G_{\text{candidate}}^{A_n}$ ,  $G_{\text{candidate}}^{A_n} = j$ 
    Call self to find next best link for feature point  $old\_j$ :
end

```

#### 2.4. Trajectory relinking

The restriction that each feature point can only be in one trajectory leads to broken trajectories when particles overlap during crossing of tracks. Relinking of trajectories is therefore required for high particle density experiments. Let  $T^A$  be a set of trajectories in  $A$ , where each trajectory contains a set of linked feature points  $\hat{p}_l$  and let  $\dim(T^A)$  be the number of trajectories in  $A$ . By applying a cost function to each trajectory combination, a cost vector  $D^{l,A} \in \mathbb{R}^{\dim(T^A)}$  can be constructed for each trajectory  $l = 1 \dots \dim(T^A)$  so that  $D_m^{l,A} = \sum_{\text{feature}} \phi_{l,m}$ , where  $m$  represents the relinking candidates in  $T^A$ . Note that due to the symmetry  $D_m^{l,A} = D_l^{m,A}$ , only  $m = l + 1 \dots \dim(T^A)$  needs to be calculated and  $D_{m=1..l}^{l,A}$  can be set to  $\infty$ .

##### 2.4.1. Features

Since trajectory relinking uses the same trajectory data as the former linking process, the five proposed features for trajectory relinking are similar to those found for feature point linking. The *first* and *last* superscripts are used to indicate the first and last feature point and their respective properties in the given trajectory. For simplification of the expressions in this section, let  $t_1$  and  $t_2$  represent respectively the first and last starting trajectory.  $t_1$  and  $t_2$  are then given for each combination  $l, m$  so that  $n_{t_2}^{first} \geq n_{t_1}^{first}$ . In order to allow trajectories to bridge a maximum of one whole feature point linking step, a scenario where a particle disappears or is unavailable for linking for  $R$  slices, the first feature given in eq. 7 is introduced.

$$\phi_{t_1, t_2}^{z\text{-order}} = \begin{cases} 0, & 0 \leq n_{t_2}^{first} - n_{t_1}^{last} \leq 2R + 1 \\ \infty, & \text{elsewhere} \end{cases} \quad 7$$

Unlikely relinking candidates are filtered using eq. 1 with  $i = t_1^{last}$ ,  $j = t_2^{first}$ ,  $d_{p,max} = d_{t,max}$ , where  $d_{t,max}$  is the user-specified maximum trajectory relinking distance.  $w_{distance}$  was set to the same user-specified value as for feature point linking.

Let  $\bar{v}_{t_1}$  and  $\bar{v}_{t_2}$  represent the average velocity vectors for respectively  $t_1$  and  $t_2$ . The averaged linking vector  $\bar{v}_{t_1,t_2}$  between the Q closest endpoint pairs in the trajectories is given by:

$$\bar{v}_{t_1,t_2} = \frac{1}{Q} \sum_{q=0}^{Q-1} \frac{1}{n_{t_2}^{first+q} - n_{t_1}^{last-q}} \begin{bmatrix} x_{t_2}^{first+q} - x_{t_1}^{last-q} \\ y_{t_2}^{first+q} - y_{t_1}^{last-q} \end{bmatrix} \quad 8$$

Where Q is the number of endpoints used for averaging which showed the best experimental results for  $Q = 3$ .

To ensure alignment between the trajectories as well as the trajectories and the linking vector, the third feature penalizes difference between these respective velocity vectors.

$$\phi_{t_1,t_2}^{\text{align}} = w_a^2 \begin{cases} f(\theta_a)^2 & |\theta_a| \leq \theta_{t,max} \ \& \ |\theta_b| \leq \theta_{t,max} \\ \infty & \text{elsewhere} \end{cases} \quad 9$$

Where  $\theta_a$  is the angle between  $\bar{v}_{t_1}$  and  $\bar{v}_{t_2}$  and  $\theta_b$  is the angle between  $(\bar{v}_{t_1} + \bar{v}_{t_2})/2$  and  $\bar{v}_{t_1,t_2}$ .  $\theta_{t,max}$  is the maximum allowed trajectory relinking angle.  $\theta_{t,max}$  was set to  $\theta_{p,max}$  in the code implementation for these experiments due to the high similarity between these parameters.

The last two features are given by the intensity and velocity features as used for feature point linking using the track averages.

#### 2.4.2. Trajectory relinking

Trajectory  $l$  is linked to trajectory  $M = \min_m D^{l,A}$  if  $D_m^{l,A} \leq D_{max}$ , where  $D_{max}$  is a user-specified maximum linking cost, usually given as a function of  $d_{t,max}$ . By merging  $l$  into  $M$ , i.e.  $\hat{p}_M = \hat{p}_l \ || \ \hat{p}_M$ , during linking, the newly merged trajectory is considered for further cost function evaluations. Due to the small number of trajectories and relinking candidates, this simplified cost minimization approach was found to be sufficient.

#### 2.5. Code implementation

The linking procedure described was implemented in Java 1.6 as part of a larger collection of FNTD related routines (the 'FNTD package') and uses various FIJI classes. Also, some MOSAIC Toolsuite classes were extended to allow for storage of the feature points and their respective information required for this method, while maintaining compatibility with the MOSAIC feature point detection routine. Execution of the Java code and analyses of the results were done using the FNTD package

(v0.8.1) for the R language (R Development Core Team 2011) (v3.2.2). The sources for both the R routines and the Java code are freely available at Github (<https://github.com/FNTD>). For Fiji, the latest version of the plugin is provided via the update site at <http://sites.imagej.net/FNTD>. Installation and usage instructions are available at [https://fntd.dkfz.de/fntd/index.php/Main\\_Page](https://fntd.dkfz.de/fntd/index.php/Main_Page).

### 3. Validation

#### 3.1. High fluence synchrotron carbon ion irradiation algorithm comparison

The improvement that can be achieved with the described algorithm is especially distinct for very complex particle fields. The benefit is illustrated at an FNTD irradiated in the rising flank of a Spread-Out Bragg Peak (SOBP) of a clinical 12-C ion beam. RW3 water equivalent plastic slabs (PTW Freiburg GmbH) were used as phantom material. The irradiation consisted of 18 separate beams leading to a SOBP located at a depth of 10 to 15 cm. The FNTD was positioned at 8.5 cm where the total particle fluence reaches a maximum. This represents a clinically relevant, but at the same time most challenging, situation for identifying trajectories due to the large amount of secondary fragments in the beam, which yield a significant variation in fluorescence intensity and track direction.

The FNTDs were read out using the Landauer FXR700RG automated reader, a CLSM dedicated to FNTD readout which uses a 100x 0.95 air objective in combination with an Avalanche Photo Diode (APD) (Akselrod et al. 2014). A readout stack of 20 images with an image size of 200x200  $\mu\text{m}^2$  (1024 x 1024 pixel) and 5  $\mu\text{m}$  separation between the slices was acquired. A zoomed section of the first slice is shown in Fig. 1.

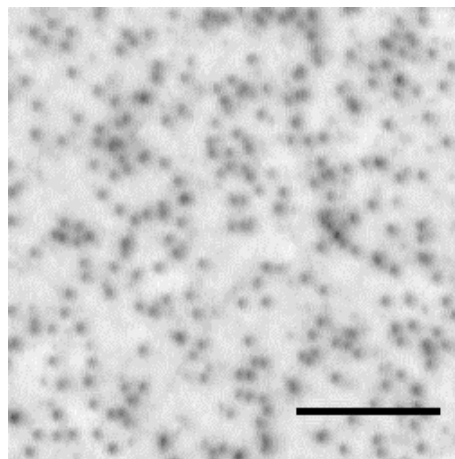


Fig. 1: 2x zoomed fluorescence image of first slice of a stack in the FNTD. The scale bar corresponds to 16  $\mu\text{m}$ .

The background was subtracted using the histogram-based ‘background subtractor’ from the MOSAIC ToolSuite (Cardinale 2010). The intensity decrease near the edges of the FOV and deeper in the sample were corrected using field-of-view non-uniformity and spherical aberration corrections as presented in (Bartz et al. 2014). Particle tracks were reconstructed both with the presented 3D feature point tracking method and with the algorithm of Sbalzani, Koumoutsakos (Sbalzarini & Koumoutsakos 2005), Levy and Incardona (Levy & Incardona 2014), from now on referred to as ‘previous method’. In both cases particle segmentation was achieved with a relative threshold of 5%, a particle radius of 3 pixels and no cut-off value in order to avoid outlier discrimination. Particle linking was performed with the parameters listed in Table 1.

Table 1: Feature point linking parameters for the 12-C irradiated samples. Values used for the two linking methods are listed separately.

Parameter	Previous method	Proposed method	Parameter	Previous method	Proposed method
$I$	5%.		$w_d$	1	1
$r = r_p$	-	4 px	$w_i$	1	1
$d_{p,max}$	15 px	15 px	$w_v$	-	1
$R$	2	2	$w_a$	-	1
$\theta_{p,max}$	-	20°	$d_{t,max}$	-	40 px
$H$	-	3	$D_{max}$	-	$0.1 \cdot C_{max}$

Since very short trajectories are likely to be caused by the linking of erroneously segmented features or the incorrect linking of true particles the minimum trajectory length was set to 5 slices.

Fig. 2 visualizes a comparison between the tracks reconstructed in sections of the image with the previous method (a,c,e) and with the proposed method (b,d,f). The images show the projection of the reconstructed tracks along the z-axis and thus correspond to a zoomed section of the readout volume.

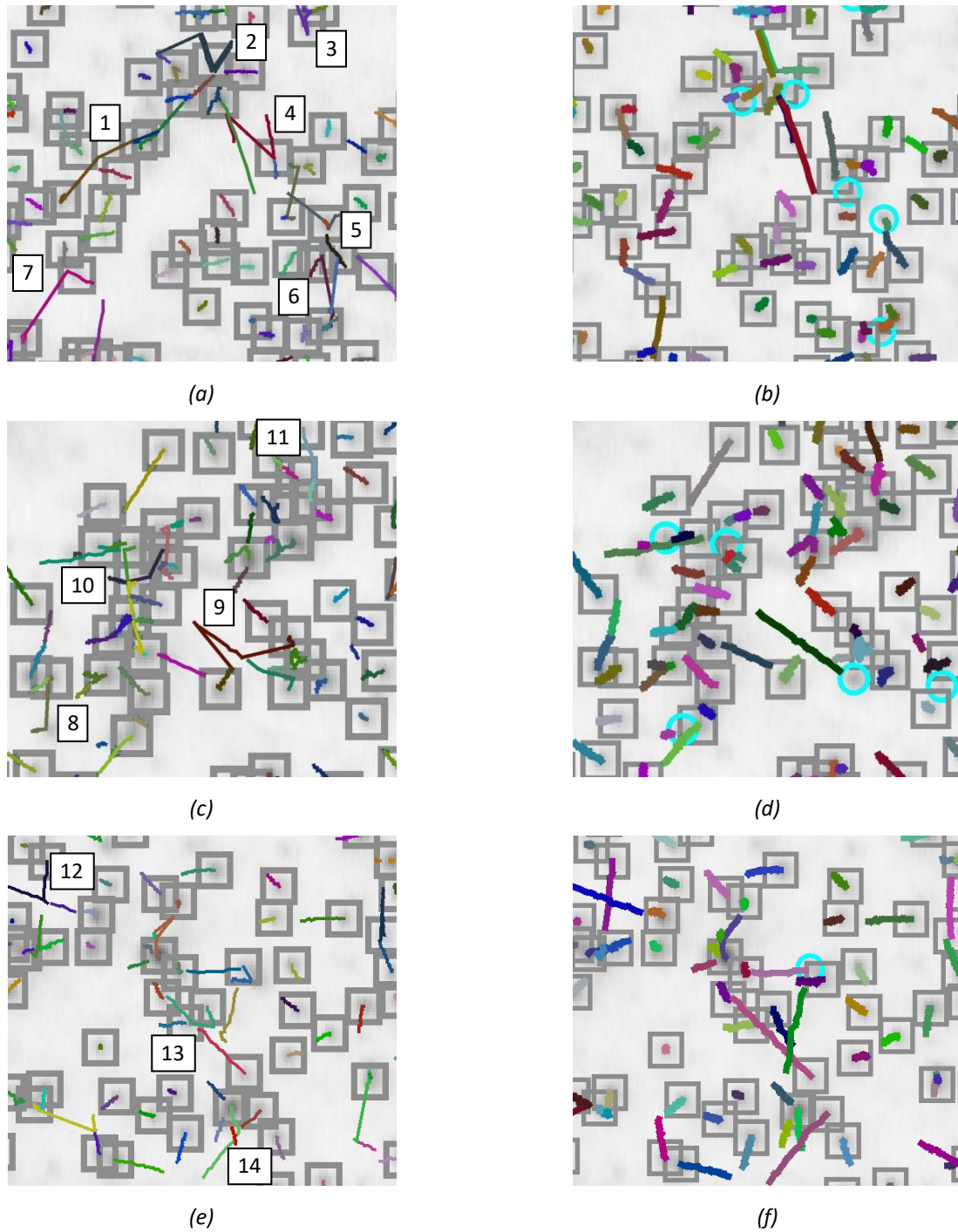


Fig. 2: Tracks produced by the implementation of Sbalzarini, Koumoutsakos, Levy and Incardona (left), compared to the proposed method (right). Gray squares indicate a tracked feature point while coloured lines indicate projections of a track. Cyan circles represent tracked feature points that were not assigned to a track. Track colours and thickness between the methods do not correspond. The numbered tracks are described in the text.

A crucial constraint for the production of physically reasonable tracks is the maximum track angle  $\theta_{p,max}$ . In the previous method this parameter was not implemented. In Fig. 2 all numbered tracks 1-10 show unphysically strong bends. With the proposed method the corresponding feature points were linked differently since the maximum allowed linking angle was set to  $20^\circ$  with respect to the average link velocity vector of the last  $H=3$  feature points. The angle threshold also prevents linking of parallel tracks like performed for track 2.

Since the presented algorithm performs a recursive minimization of the cost function instead of an assignment problem approach all feature points are more likely to be linked to the best linking candidate. The different approaches can for example result in an altered assignment of feature points to tracks as in location 11. The points belonging to the green and pink tracks are also considered in the presented algorithm but distributed differently among the two tracks.

The choice and interplay of features included into the cost function in the presented method leads to a strongly improved reconstruction of crossing trajectories compared to the previous method. This effect is very beneficial for experiments with complex high fluence particle fields. Improved linking can e.g. be seen for tracks 12, 13 and 14 in the bottom row of Fig. 2.

As described in section 2.4 the proposed method enables relinking of trajectories with very similar features. Tracks break apart if corresponding feature points are tracked incompletely. This occasionally happens with tracks of secondary particles with low fluorescence intensity and large track angles with respect to the z-axis or crossing tracks which overlap in one or more image slices. As shown in the top row of Fig. 3 the benefit for linking of crossing tracks compared to the previous method (cf. bottom row of Fig. 2) is partly due to the implementation of track relinking (track 13 and 14). The bottom row of Fig. 3 shows another comparison between the linking results without (a,c) and with (b,d) relinking for crossing trajectories (15 and 16) and for a secondary particle track (17).

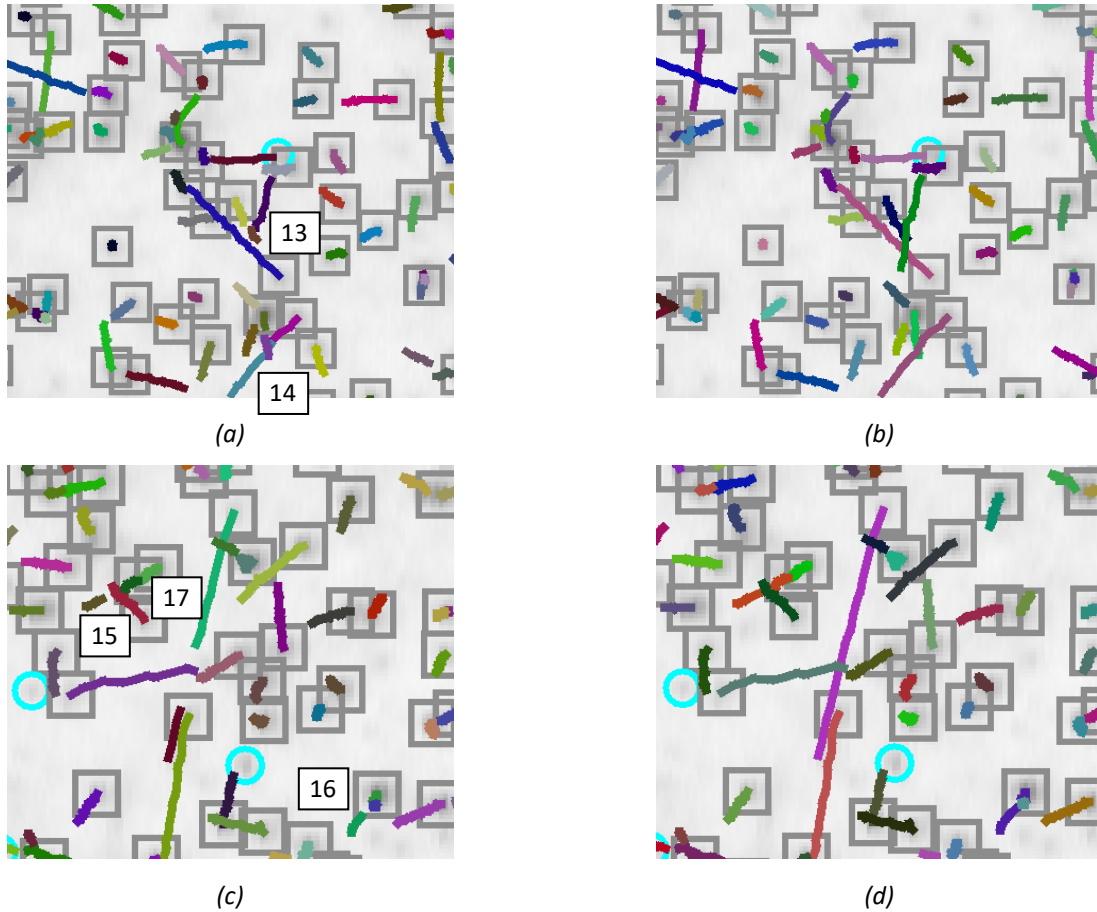


Fig. 3: Tracks produced by the proposed algorithm with (left) and without relinking (right). The numbered features are explained in the text.

### 3.2. Am-241 alpha radiation energy estimation

An FNTD was irradiated from the top with a circular Am-241 source, with  $r_{\text{source}} \gg r_{\text{FNTD}}$  and 2.5 mm air between the source and the FNTD so that the irradiation was unidirectional. The expected fluence in the FNTD was  $1.25 \times 10^6 \text{ cm}^{-2}$ , which corresponds roughly to the scenario of a cell study with 1 alpha track per 10  $\mu\text{m}$  diameter cell. The FNTD was read-out using a Carl Zeiss LSM710 with a 63x 1.40 oil-immersion objective and two fiber-coupled, photon-counting APDs (Klimpi et al. 2015). 6 separate image stacks, each containing 42 slices, were obtained. Each image slice contained 1024 x 1024 pixels with pixel dimensions 0.13 x 0.13 x 0.47  $\mu\text{m}^3$  (x, y, z). The surface location was obtained via measurement of the surface reflection using the second APD parallel to the fluorescent measurement.

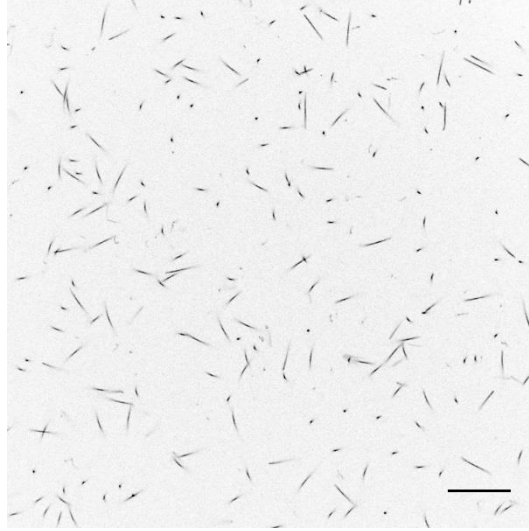


Fig. 4: FNTD irradiated with alpha particles produced by the decay of Am-241. Note the wide variety of incidence angles (as seen from the elongated shapes), the crossing of tracks and presence of highly energetic delta rays. The scale bar corresponds to 16  $\mu\text{m}$ .

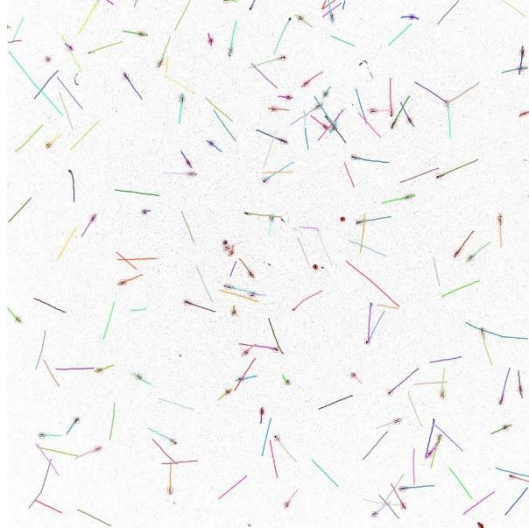
Feature point detection was performed with an absolute threshold just above the background noise threshold and a relatively large feature point radius of 6 pixels, as to prevent the detection of multiple feature points within an elongated spot. Again, the cut-off value was not set in order to avoid outlier discrimination. The feature point linking routine was executed with the parameters given in Table 2.

Table 2: Feature point linking parameters for Am-241 irradiation linking.

Parameter	Value	Parameter	Value
$I$	35 a.u.	$w_d$	0.5
$r = r_p$	5 px	$w_i$	1
$d_{p,max}$	30 px	$w_v$	0.1
$R$	3	$w_a$	1
$\theta_{p,max}$	20°	$d_{t,max}$	50 px
$H$	5	$D_{max}$	$1 \cdot C_{max}$

Since the feature point detection routine was built for circular spots, ion tracks with very high angles of incidence led to detection and linking artefacts due to their elongated appearance. Tracks spanning less than 8 slices or with fitted angles  $\theta > 50$  degrees were therefore removed. When inclusion of these tracks is critical for the user, more sophisticated, and computationally intensive,

detection algorithms are available which to recognize more complex shapes (Rizk et al. 2014; Arganda-Carreras et al. 2014). However, extra effort is required to make these algorithms output the feature points in a compatible format.



*Fig. 5: Linking of the sample in Fig. 4 with the parameters in Table 2. Squares and circles indicate respectively linked and unlinked feature points. Feature points are correctly linked in crowded areas and no artefacts are visible. The elongated spots from particles with very high angles of incidence led to detection of multiple feature points.*

The reference fluence  $\Phi_{\text{adj}}$  was calculated taking into account the maximum angle of acceptance  $\theta$ :

$$\Phi_{\text{adj}}(\theta) = \Phi \cdot (1 - \cos \theta) \quad 10$$

where  $\Phi$  is the fluence for the entire hemisphere (solid angle =  $\pi$ ). A total of 509 tracks was found after filtering, while the adjusted reference fluence was  $489 \pm 44$ . A total of 39 tracks originated from trajectory relinking, exemplifying the significance of this added routine.

For further analysis of the tracks, tracks ending close to the border of the image were removed, due to their likelihood having a part of the track lying out of bounds, thereby appearing as an artefact. The penetration length of each track was calculated from the incidence angle and the depth of the last feature point in respect to the surface. Refinement of the exact endpoint was based on the intensity of the last few feature points. Knowing the penetration depth and the thickness of the layer of air, the total traversed distance and thereby the equivalent range in water for each track could be calculated. The range in water to initial kinetic energy translation table was obtained using SRIM (Ziegler 2013). The resulting calculated initial alpha kinetic energy was  $5451 \pm 310$  keV (Fig. 6).

The limited z-resolution, energy loss straggling, detector noise and the unknown thickness of the activity layer added to the uncertainty. However, artefact can be identified as tracks with a measured energy far away from the given distribution curve relating incident angle and length. From Fig. 6 it was estimated that this was the case for less than 1% of the reconstructed trajectories.

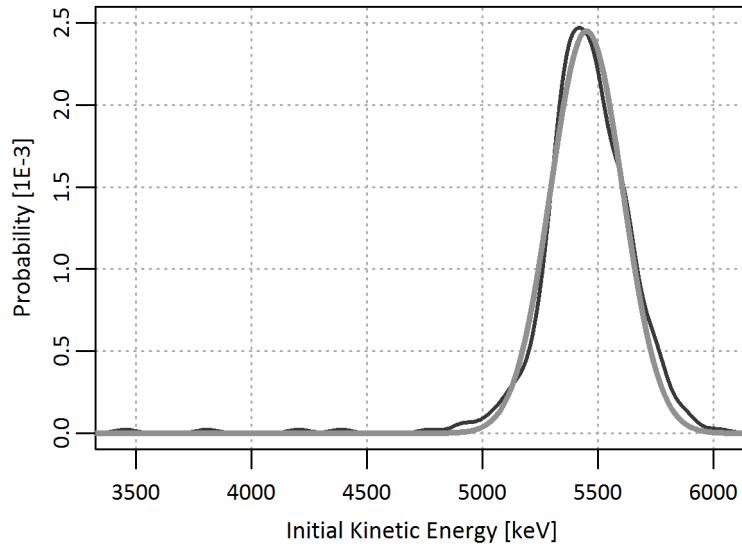


Fig. 6: The calculated initial kinetic energy distribution in dark grey with the Gaussian fit shown in light gray.

### 3.3. Parameter Sensitivity Analysis and Usability

A one-at-a-time parameter sensitivity analysis was performed on the experimental data given in section 3.2. The effect of varying each parameter on the fitted mean energy, fluence and RMSE of the fit were measured while the rest of the parameters was as given Table 2. The detailed results are given in Appendix A. In summary, it was found that the 13 parameters can be subdivided in two general categories: fine-tuning parameters, parameters that (mildly) influence the algorithm over a wide range, and threshold parameters, parameters that influence the algorithm only from a specific value, similar to an on/off-switch (Table 3). The algorithm proved to be stable and failed only when critical aspects were disabled. For example, setting the maximum linking distance to very small values yielded a large deviation from the expected behaviour. Most of variables are robust and serve a role in fine-tuning the algorithm to obtain the best results for the specific application. Some parameters reflect a physical property and can be estimated using the available data, namely intensity threshold  $I$ , particle radius  $r$ , maximum displacement  $d_{p,max}$ , particle drift  $r_p$ , maximum linking angle  $\theta_{p,max}$  and the maximum trajectory relinking distance  $d_{t,max}$ . The remaining seven

parameters require an initial guess from the user. Three of these parameters, namely distance weight  $w_d$ , angle weight  $w_a$  and relink cost  $D_{max}$  are threshold values and therefore require manual iterating to find their working values. This can be done quickly and interactively using the Fiji implementation. The remaining four parameters are fine-tuning parameters and are expected to be work over a wide range of values.

While the number of parameters can in principle be reduced given the above findings and using default values for specific applications, they provide the experienced user with flexibility.

Table 3: Parameter properties

Category	Parameter	Type	Sensitivity	Reflects physical property
<i>Feature Point</i>	$I$	Fine-tuning	Strong	Yes
<i>Selection</i>	$r$	Fine-tuning	Strong	Yes
<i>Feature Point</i>	$d_{p,max}$	Threshold	-	Yes
<i>Linking</i>	$R$	Fine-tuning	Low	No
	$r_p$	Fine-tuning	Mild	Yes
	$\theta_{p,max}$	Fine-tuning	Mild	Yes
	$H$	Fine-tuning	Low	No
	$w_d$	Threshold	-	No
	$w_i$	Fine-tuning	Low	No
	$w_v$	Fine-tuning	Strong	No
	$w_a$	Threshold	-	No
<i>Trajectory Relinking</i>	$d_{t,max}$	Threshold	-	Yes
	$D_{max}$	Threshold	-	No

#### 4. Conclusion

The combination of an iterative cost minimization function and a trajectory relinking algorithm in addition to a specialized cost function aimed at favouring constant trajectories, resulted in a fast and accurate algorithm for single ion track reconstruction that could be validated for both high and low fluence samples. Linking of particles and relinking of trajectories using one thread for 45000 (2900) particles took 4.43 (0.16) seconds on an Intel(R) Core(TM) i5-560M 2.67 GHz processor, compared to 32.16 (13.25) seconds for the old implementation. The high fluence SOBP carbon-12 experiment tested the algorithm for high fluences with up 2000 tracks per 512x512 pixel image, a

scenario that could not be tracked reliably with existing methods. A clear increase in fragmentations was visible, despite their high angles of incidence and relatively low SNR. It is expected that these fluences are at the limit of this algorithm, partly due to difficulty of detecting the correct feature points for these scenarios. The low fluence Am-241 alpha irradiation experiment showed a low artefact count with less than 1% faulty trajectories and a calculated fluence that closely matched the expected value. It was found that most input variables could be chosen intuitively by the user and an appropriate set of parameters could usually be found within one or two iterations. The Fiji plugin allows for easy and quick optimization of the linking parameters without the need for prior programming knowledge, while the R shell is best used for linking of larger sample sets and trajectory data analyses.

### **Acknowledgements**

The authors are grateful to Dr. Mark Akselrod and Landauer Inc. for kindly donating the FNTDs and Shirin Rhamanian for conducting the Monte Carlo transport simulation. We also greatly appreciate the continuous support by Dr. Ivo Sbalzarini and Pietro Incardona, the Max Planck Institute of Molecular Cell Biology and Genetics, providing details and a customized version of the Mosaic ToolSuite. Furthermore, we gratefully acknowledge STW for funding (project number 13577).

### **References**

- Akselrod, G.M. et al., 2006. A novel Al<sub>2</sub>O<sub>3</sub> fluorescent nuclear track detector for heavy charged particles and neutrons. *Nuclear Instruments and Methods in Physics Research, Section B: Beam Interactions with Materials and Atoms*, 247(2), pp.295–306.
- Akselrod, M.S. et al., 2014. Automatic neutron dosimetry system based on Fluorescent Nuclear Track Detector Technology. *Radiation Protection Dosimetry*, 161(1), pp.86–91.
- Arganda-Carreras, I. et al., 2014. Trainable Weka Segmentation : A Machine Learning Tool for Microscopy Image Segmentation.
- Bartz, J.A. et al., 2014. High resolution charge spectroscopy of heavy ions with FNTD technology. *Nuclear Instruments and Methods in Physics Research, Section B: Beam Interactions with Materials and Atoms*, 335, pp.24–30. Available at: <http://dx.doi.org/10.1016/j.nimb.2014.05.019>.
- Cardinale, J., 2010. Histogram-based background subtractor for ImageJ. , (1983), pp.1–4. Available at: [www.mosaic.ethz.ch](http://www.mosaic.ethz.ch).
- Chetverikov, D. & Verestói, J., 1999. Feature Point Tracking for Incomplete Trajectories. *Computing*, 62(4), pp.321–338. Available at: <http://www.springerlink.com/openurl.asp?genre=article&id=doi:10.1007/s006070050027>  
<http://dx.doi.org/10.1007/s006070050027>.

- Elgqvist, J. et al., 2014. The Potential and Hurdles of Targeted Alpha Therapy – Clinical Trials and Beyond. *Frontiers in Oncology*, 3(January), pp.1–9. Available at: <http://journal.frontiersin.org/article/10.3389/fonc.2013.00324/abstract>.
- Grad, M. et al., 2012. An ultra-thin Schottky diode as a transmission particle detector for biological microbeams. *Journal of instrumentation : an IOP and SISSA journal*, 7, pp.1–22. Available at: <http://www.pubmedcentral.nih.gov/articlerender.fcgi?artid=3776448&tool=pmcentrez&rendertype=abstract>.
- Hanin, L. & Zaider, M., 2014. On the probability of cure for heavy-ion radiotherapy. *Physics in Medicine and Biology*, 59(14), pp.3829–3842. Available at: <http://stacks.iop.org/0031-9155/59/i=14/a=3829?key=crossref.4aa4ff069c7fcf43c4b80e3a5277cbdd>.
- Hei, T.K. et al., 2009. Advances in radiobiological studies using a microbeam. *Journal of radiation research*, 50 Suppl A(0 0), pp.A7–A12.
- Jadvar, H. & Quinn, D.I., 2013. Targeted  $\alpha$ -particle therapy of bone metastases in prostate cancer. *Clinical nuclear medicine*, 38(12), pp.966–71. Available at: <http://www.scopus.com/inward/record.url?eid=2-s2.0-84888303650&partnerID=tZOtx3y1>.
- Klimpi, G.M., Mescher, H. & Akselrod, M.S., 2015. *Fluence-based dosimetry of therapeutic ion beams using single track detectors*,
- Kratochwil, C. et al., 2014.  $^{213}\text{Bi}$ -DOTATOC receptor-targeted alpha-radionuclide therapy induces remission in neuroendocrine tumours refractory to beta radiation: a first-in-human experience. *European Journal of Nuclear Medicine and Molecular Imaging*, 41(11), pp.2106–2119. Available at: <http://link.springer.com/10.1007/s00259-014-2857-9>.
- de Kruijff, R., Wolterbeek, H. & Denkova, A., 2015. A Critical Review of Alpha Radionuclide Therapy—How to Deal with Recoiling Daughters? *Pharmaceuticals*, 8(2), pp.321–336. Available at: <http://www.mdpi.com/1424-8247/8/2/321/>.
- Levy, G. & Incardona, P., 2014. MOSAIC ParticleTracker 2D and 3D.
- Loeffler, J.S. & Durante, M., 2013. Charged particle therapy—optimization, challenges and future directions. *Nature reviews. Clinical oncology*, 10(7), pp.411–424.
- Luo, N. et al., 2015. A Novel Tracking Algorithm via Feature Points Matching. *Plos One*, 10(1), p.e0116315. Available at: <http://dx.plos.org/10.1371/journal.pone.0116315>.
- Nelson, B., 2015. A beam of hope for heavy ion radiotherapy: Promising clinical results and better designs are adding new momentum to the push for more proton and carbon ion radiotherapy centers. *Cancer Cytopathology*, 123(8), pp.445–446. Available at: <http://doi.wiley.com/10.1002/cncy.21598>.
- Niklas, M., Greilich, S., et al., 2013. Engineering cell-fluorescent ion track hybrid detectors. *Radiation oncology (London, England)*, 8, p.141. Available at: <http://www.pubmedcentral.nih.gov/articlerender.fcgi?artid=3699405&tool=pmcentrez&rendertype=abstract>.
- Niklas, M., Bartz, J.A., et al., 2013. Ion track reconstruction in 3D using alumina-based fluorescent

nuclear track detectors. *Physics in medicine and biology*, 58(18), pp.N251–66. Available at: <http://www.ncbi.nlm.nih.gov/pubmed/23965401>.

Niklas, M., Melzig, C., et al., 2013. Spatial correlation between traversal and cellular response in ion radiotherapy - Towards single track spectroscopy. *Radiation Measurements*, 56, pp.285–289. Available at: <http://dx.doi.org/10.1016/j.radmeas.2013.01.060>.

Prise, K.M. & Schettino, G., 2011. Microbeams in radiation biology: Review and critical comparison. *Radiation Protection Dosimetry*, 143(2-4), pp.335–339.

R Development Core Team, 2011. *R: A Language and Environment for Statistical Computing*, Vienna, Austria: the R Foundation for Statistical Computing.

Rizk, A. et al., 2014. Segmentation and quantification of subcellular structures in fluorescence microscopy images using Squash. *Nature protocols*, 9(3), pp.586–96. Available at: <http://www.ncbi.nlm.nih.gov/pubmed/24525752>.

Sartor, O. et al., 2012. Targeted use of Alpha Particles: Current Status in Cancer Therapeutics. *Journal of Nuclear Medicine & Radiation Therapy*, 03(04). Available at: <http://www.omicsonline.org/targeted-use-of-alpha-particles-current-status-in-cancer-therapeutics-2155-9619.1000136.php?aid=8339>.

Sbalzarini, I.F. & Koumoutsakos, P., 2005. Feature point tracking and trajectory analysis for video imaging in cell biology. *Journal of Structural Biology*, 151(2), pp.182–195.

Schettino, G., Al Rashid, S.T. & Prise, K.M., 2010. Radiation microbeams as spatial and temporal probes of subcellular and tissue response. *Mutation Research - Reviews in Mutation Research*, 704(1-3), pp.68–77.

Schindelin, J. et al., 2012. Fiji: an open-source platform for biological-image analysis. *Nature Methods*, 9(7), pp.676–682. Available at: <http://rsbweb.nih.gov/ij/docs/guide/user-guide.pdf>.

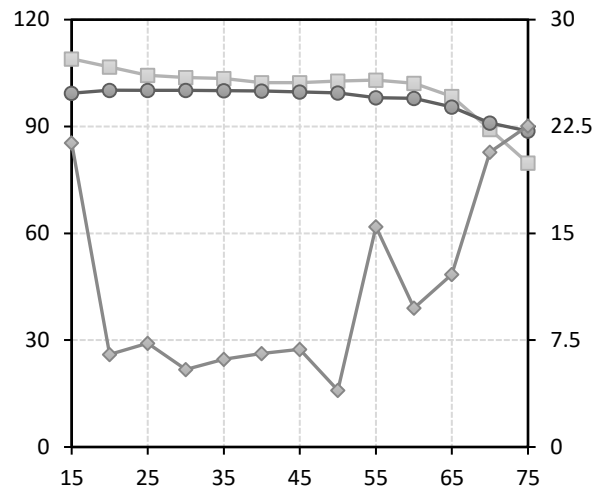
Schneider, C. a, Rasband, W.S. & Eliceiri, K.W., 2012. NIH Image to ImageJ: 25 years of image analysis. *Nature Methods*, 9(7), pp.671–675.

Ziegler, J., 2013. SRIM – The stopping and range of ions in matter. Version 2013.00.

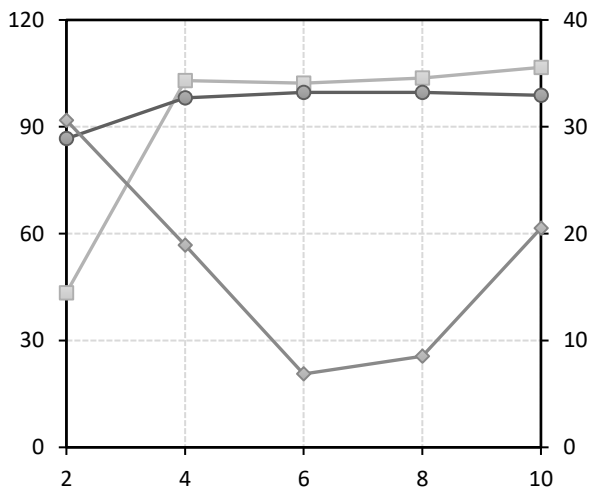
## Appendix A

- Fluence (% , left)
- Fitted Mean Energy (% , left)
- ◆— RMSE (a.u., right)

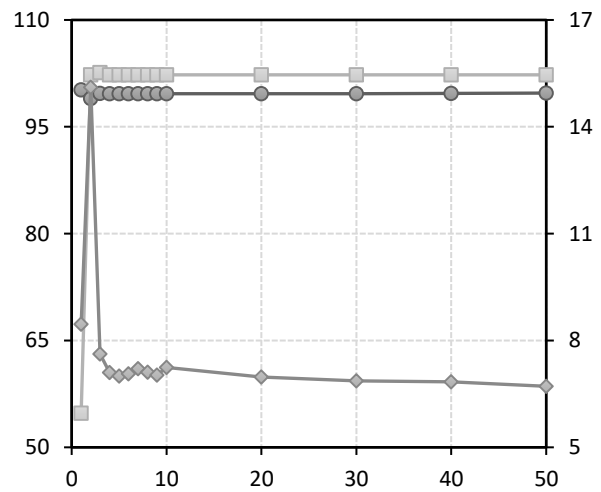
Fluence and the fitted mean energy are given as percentage of their expected value and are displayed on the left axis. RMSE is given in arbitrary units, given on the right axis, and serves as an indicator of the goodness-of-fit. A high RMSE in combination with a high or low fitted mean energy indicates a large number of faulty tracks.



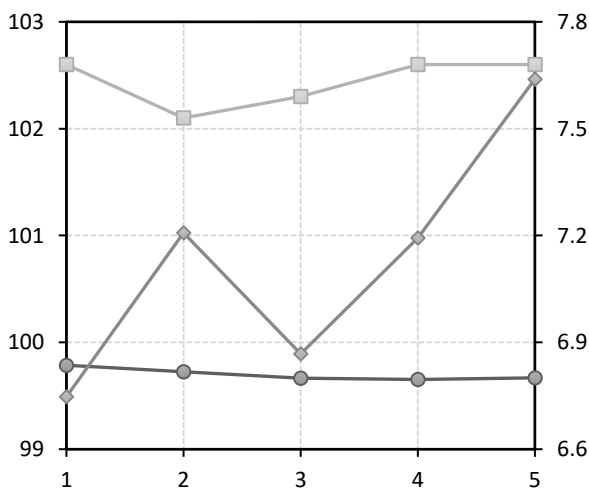
Intensity Threshold  $I$  (a.u.) – Fine Tuning



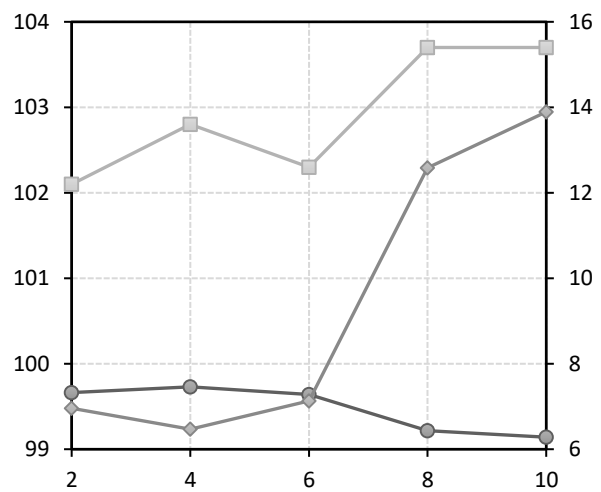
Particle Radius  $r$  (px) – Fine Tuning



Maximum Distance  $d_{p,max}$  (px) – Threshold



Linkrange  $R$  (slices) – Fine Tuning



Particle Drift  $r_p$  (px) – Fine Tuning

